Experimental measurement of $^{12}C + {}^{16}O$ fusion at stellar energies

X. Fang,[1,2] W. P. Tan,[1,*] M. Beard,[1] R. J. deBoer,[1] G. Gilardy,[1] H. Jung,[1] Q. Liu,[1] S. Lyons,[1] D. Robertson,[1] K. Setoodehnia,[1] C. Seymour,[1] E. Stech,[1] B. Vande Kolk,[1] M. Wiescher,[1] R. T. deSouza,[3] S. Hudan,[3] V. Singh,[3] X. D. Tang,[4] and E. Uberseder[5]

[1]*Institute for Structure and Nuclear Astrophysics and Joint Institute for Nuclear Astrophysics, University of Notre Dame, Notre Dame, Indiana 46556, USA*

[2]*Sino-French Institute of Nuclear Engineering and Technology, Sun Yat-Sen University, Zhuhai 519082, People's Republic of China*

[3]*Department of Chemistry and Center for Exploration of Energy and Matter, Indiana University, Bloomington, Indiana 47405, USA*

[4]*Institute of Modern Physics, Chinese Academy of Science, Lanzhou, Gansu 730000, People's Republic of China*

[5]*Cyclotron Institute, Texas A&M University, College Station, Texas 77843, USA*

(Received 9 September 2016; revised manuscript received 3 April 2017; published 9 October 2017)

The total cross section of the $^{12}C + {}^{16}O$ fusion reaction has been measured at low energies to investigate the role of this reaction during late stellar evolution burning phases. A high-intensity oxygen beam, produced by the 5 MV pelletron accelerator at the University of Notre Dame, impinged on a thick, ultrapure graphite target. Protons and γ rays were simultaneously measured in the center-of-mass energy range from 3.64 to 5.01 MeV for singles and from 3.73 to 4.84 MeV for coincidence events, using silicon and Ge detectors. Statistical model calculations were employed to interpret the experimental results. The emergence of a new resonance-like broad structure and a decreasing trend in the S-factor data towards lower energies (opposite to previous data) are found for the $^{12}C + {}^{16}O$ fusion reaction. Based on these results the uncertainty range of the reaction rate within the temperature range of late stellar burning environments is discussed.

DOI: 10.1103/PhysRevC.96.045804

I. INTRODUCTION

The fusion of light nuclei at sub-barrier energies plays an important role in the evolution of massive stars, as well as in the ignition of type Ia supernova [1,2] and the ignition of explosive burning processes in the atmospheres of accreting neutron stars [3,4]. The cross sections of fusion reactions are governed by the penetrability of the nuclei through the Coulomb and orbital angular momentum barriers, and therefore drop off exponentially with decreasing energy. This translates into extremely low values of the cross section near and within the energy range of astrophysical interest, i.e., the Gamow window. The direct experimental study of fusion reactions at stellar energies is therefore extremely difficult.

Carbon burning and oxygen burning in massive stars ($M \geqslant 8M_{\odot}$) [1] are important burning phases in late stellar evolution following helium burning as well as in cataclysmic burning phases of type Ia supernovae. In both cases the critical reactions are the $^{12}C + {}^{12}C$, $^{12}C + {}^{16}O$, and $^{16}O + {}^{16}O$ fusion processes. Extensive efforts, both experimentally and theoretically, have been invested in the determination of the reaction rates for all associated reaction channels [1,2]. Despite these efforts, large uncertainties remain in the reaction rates due to the extrapolation of the data into the Gamow range [5]. The predicted rates depend sensitively on adopted model parameters, hindrance effects, and the possibility of cluster or molecular resonances at relevant energies [2,6,7].

Extending and improving the quality of experimental data towards lower energies is therefore crucial for reducing the uncertainties—in particular, the uncertainty associated with extrapolating the data towards lower energies—and providing more reliable reaction rates for the study of late stellar evolution. The $^{12}C + {}^{16}O$ reaction plays a particularly important role in both the carbon and oxygen burning phases of stars [8,9]. Core and shell carbon burning is expected to be dominated by the $^{12}C + {}^{12}C$ fusion reaction, yet near the end of the carbon burning phase the abundance of ^{16}O in the ashes of stellar helium burning is substantially higher than that of ^{12}C, due to the $^{12}C(\alpha,\gamma)^{16}O$ reaction [10,11]. With a high abundance of ^{16}O and a competitive reaction rate, the $^{12}C + {}^{16}O$ reaction could play an important role in shell carbon burning nucleosynthesis. A similar situation exists in oxygen burning, which is dominated by the $^{16}O + {}^{16}O$ fusion. Temperature and density increase towards the final stage of this burning phase will enable the photodissociation of ^{16}O to occur, which results in the release of free ^{12}C into the hot burning environment. The produced ^{12}C will be consumed either by reacting with itself or with ^{16}O, affecting the transition to subsequent stellar burning, when intershell mixing processes transfers carbon into the oxygen burning shell of a pre-supernova star [12]. Type Ia supernovae (SN) are interpreted as the consequence of explosive carbon burning ignited near the core of white dwarf stars. The $^{12}C + {}^{12}C$ fusion process is supposed to be the dominant energy source for pre-ignition processes such as carbon simmering and the ignition itself; however, the $^{12}C + {}^{16}O$ reaction may also play a significant role depending on the associated fusion rates and the environmental conditions such as ^{16}O abundance, temperature, and density [2,13]. Recent studies showed indeed that the $^{12}C + {}^{16}O$ rate is expected to have an unusually large effect on the calcium and sulfur yields in type Ia SN; e.g., the higher $^{12}C + {}^{16}O$ rate suppresses the alpha-particle abundance, which in turn decreases the Ca/S ratio [13].

The study of the total low energy fusion cross section of the $^{12}C + {}^{16}O$ reaction is therefore of similar importance as the measurements of the competing $^{12}C + {}^{12}C$ and $^{16}O + {}^{16}O$

*wtan@nd.edu

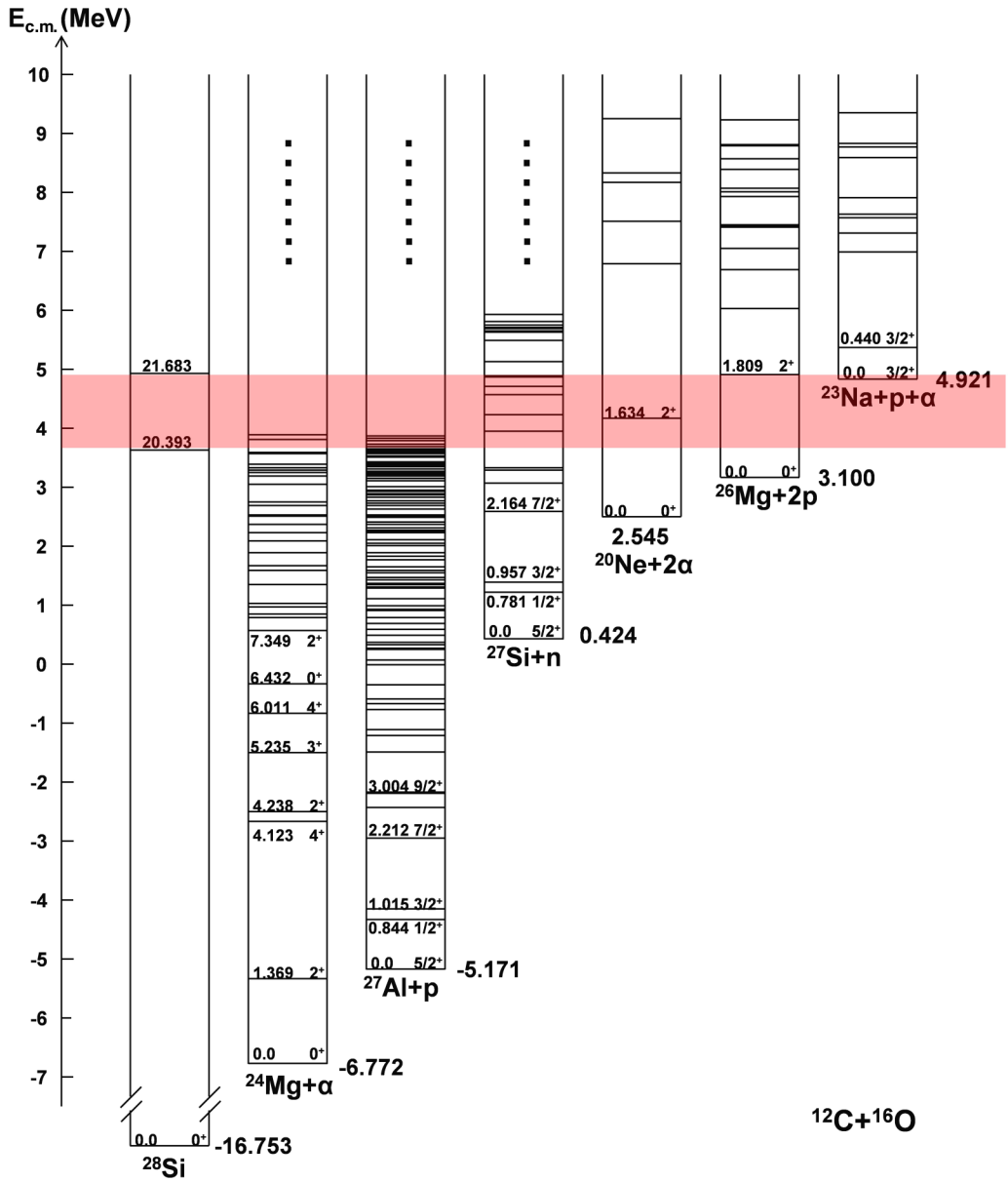

FIG. 1. The level scheme of possible open exit channels with regard to $^{12}C + ^{16}O$ fusion. The shaded area corresponds to the energy range covered in this work.

fusion reactions. The relevant stellar energy range spans from 3.0 to 7.2 MeV. The level scheme of all possible open exit channels with regard to the $^{12}C + ^{16}O$ fusion reaction is shown in Fig. 1. The three main channels of $^{12}C(^{16}O,p)^{27}Al$ ($Q = 5.170$ MeV), $^{12}C(^{16}O,\alpha)^{24}Mg$ ($Q = 6.772$ MeV), and $^{12}C(^{16}O,n)^{27}Si$ ($Q = -0.424$ MeV) reactions populate excited states in the residual nuclei that subsequently decay by γ emission to the ground state. The contribution of the $^{27}Si + n$ channel is expected to represent only a small percentage of the total reaction cross section at low energies because of its negative Q value. This is similar to the case of the $^{23}Mg + n$ channel in the $^{12}C + ^{12}C$ fusion process [14]. But as in the case of $^{12}C + ^{12}C$ fusion, the $^{12}C(^{16}O,n)^{27}Si$ reaction branch may release additional neutrons for an s-process component in carbon shell burning.

In previous studies, $^{12}C + ^{16}O$ fusion has been investigated down to energies of $E_{c.m.} = 3.9$ MeV through the γ decay of the excited states of the residual nuclei populated in the fusion process [15,16]. These experiments were complemented by the measurement of the emitted charged particles down to energies of $E_{c.m.} = 4.54$ MeV [17]. A recent test experiment using the particle-γ coincidence technique was conducted for the $^{12}C + ^{12}C$ reaction [18]. The present work is aimed at a combined study of charged particles as well as γ channels in both single and coincidence modes. To the best of our knowledge, however, no experiments have been performed to study the $^{12}C + ^{16}O$ reaction with the detection of both charged particles and γ rays in coincidence. The present experiment provides new low energy data on the $^{12}C + ^{16}O$ fusion reaction that will improve the experimental basis towards a more

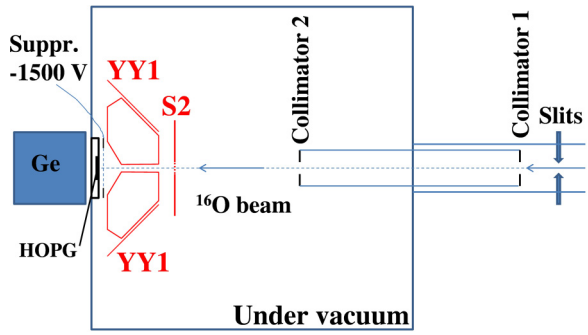

FIG. 2. The experimental setup showing the location of the charged particle as well as the γ detectors. The ^{16}O beam direction is from right to left with scattering being suppressed by a set of collimators and slits. Six YY1-type and one S2-type silicon detectors were used for the detection of charged particles. One HPGe or one NaI detector was placed immediately after the HOPG target for measuring γ rays.

reliable extrapolation and determination of the reaction rates. Many of the previous theoretical extrapolations for the total rate rely on the application of a potential model formalism [15–17]. Apart from the possible resonance structures associated with quasimolecular configurations, the observed selective population of ^{24}Mg, ^{27}Al, and ^{27}Si excited states can be explained in the framework of a compound nuclear reaction mechanism [19,20]. Hauser-Feshbach (HF) statistical-model calculations [21] have therefore been performed to interpret the observed branching ratios of the different channels, and to extract the relative population possibilities of unobserved reaction branches.

II. EXPERIMENTAL PROCEDURE

In this work both charged particles (mainly proton) and γ rays emitted from the $^{12}C + ^{16}O$ fusion process were measured simultaneously. A beam of $^{16}O^{5+}$, $^{16}O^{3+}$ ions produced by the ECR source of the Stable beam Accelerator for Nuclear Astrophysics (St. ANA) was used to bombard a thick graphite target. The St. ANA accelerator is a 5 MV single-ended Pelletron accelerator at the Nuclear Science Laboratory (NSL) of the University of Notre Dame. This accelerator provides high intensity (at least tens of particle μA) heavy ion beams, up to ^{40}Ar. The target was highly ordered pyrolytic graphite (HOPG) [22], which has a layered structure of multiple thin graphene sheets [23]. The advantage of using HOPG as target material is its superior purity compared to natural graphite. The heavy elemental impurities (Ba, Fe, Ca, and so on) in graphite can cause scattering of the ^{16}O beams, producing background in the silicon detector array. A first test measurement demonstrated that the background level of HOPG in a silicon detector was $\sim$1% of that observed with natural graphite. A HOPG target with a dimension of 2 cm $\times$ 2 cm $\times$ 1 mm was attached to a water-cooled aluminum holder and fixed by a round graphite disk with a rectangular hole in the center. One electrically isolated graphite ring with a negative voltage of 1500 volts was used to suppress secondary electrons from the target [24]. This suppression ensured accurate reading of the beam current.

The experimental setup is shown in Fig. 2. The silicon-detector array consists of six YY1-type silicon detectors and one S2-type silicon detector [25], covering angles from 102° to 146° and 151° to 170° in the laboratory frame. Each wedge-shaped YY1 is segmented into 16 strips on the front junction side with six of them forming a "lampshade" configuration. The CD-shaped S2 detector is doubled sided and has 48 rings on the front junction side and 16 segments on the back Ohmic side. The solid angle covered by the detectors is 4.1% of 4π for each YY1, and 5.4% of 4π for the S2. For the measurement of the γ transitions, high purity germanium (HPGe) and NaI detectors were used. They were alternatively positioned right behind the target to maximize the detection efficiency of γ rays. For the final measurement the HPGe detector was used. The energy and efficiency of the HPGe detector were determined by using calibrated ^{60}Co, ^{137}Cs, and ^{152}Eu sources. The absolute γ peak efficiencies were determined to be 1.74% at 844 keV, 1.68% at 1014 keV and 1.50% at 1368 keV. The test with the radioactive sources shows a small summing effect (less than 5%). Most of the γ rays from the reaction channels of interest are not affected by the summing effect as they correspond to a direct decay of the populated states to the ground state of the final nucleus. For the few affected γ rays, other uncertainties such as statistical errors are much larger, making the summing corrections negligible. To protect the silicon detectors from the high intensity scattered beam particles, a set of graphite collimators were installed along the beam axis. Graphite was superior to heavier metal collimators because it reduced significantly large-angle beam scattering. The data were collected by the VMUSB data acquisition system implemented at NSL, where 160 channels of signals from the silicon detector array were processed via an ASIC (application specific integrated circuit) readout system. The core component of the system is HINP16C, a 16-channel ASIC specifically developed for readout of silicon strip detectors used in low- and intermediate-energy heavy-ion reactions [26]. The HPGe detector was read out by the 13-bit high resolution analog-to-digital converter (ADC) from Mesytec [27].

$^{16}O^{3+}$ beams with energies from 8.5 to 11.7 MeV were used to bombard the target in steps of 100 or 200 keV. This corresponds to an energy range of $3.64 \leqslant E_{c.m.} \leqslant 5.01$ MeV in the center-of-mass system. For testing the detector array, higher energy $^{16}O^{5+}$ beams were used at 15.0 and 16.0 MeV. For probing the beam-induced background, data were taken at low energy $E_{\text{beam}} = 7.0$ MeV ($E_{c.m.} = 3.0$ MeV). In front of the YY1 silicon detectors, a thin Mylar foil (3.6 μm) was attached to protect the silicon from scattered beam particles; thicker aluminum foil (44 μm) was also used to stop α particles with energies up to about 8 MeV for some detectors in some of the runs, although some of the most energetic α particles from the ^{24}Mg ground state channel could still leak into the low energy end of the spectra. The S2 detector was shielded in a similar fashion. At higher beam energies and intensities, some of the detectors were handicapped by large leakage currents, presumably caused by beam induced x rays. Simultaneously with particle detection, γ rays from all reaction channels were measured by the NaI detector at higher beam energies $E_{\text{beam}} \geqslant 11.3$ MeV(that does not separate background from peaks of interest well and therefore are not reported in this work) and

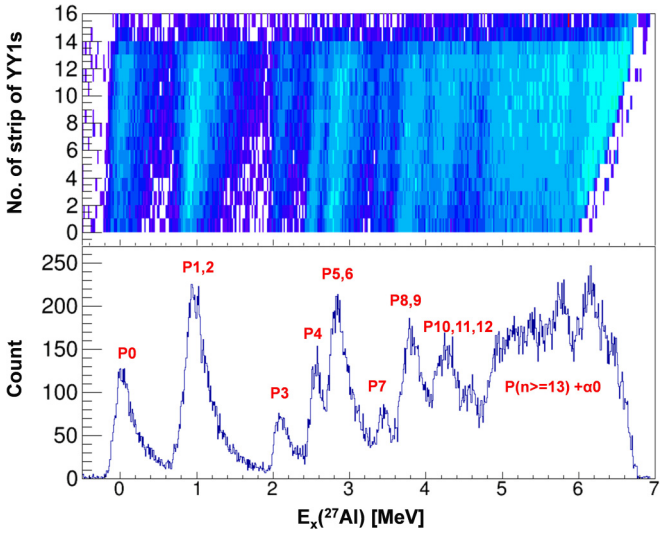

FIG. 3. Proton spectrum of ^{12}C(^{16}O, p)^{27}Al reaction taken by YY1s at $E_{\rm beam} = 11.3$ MeV. The top panel shows the raw spectrum of YY1s for the different strips versus excitation energies in ^{27}Al. The bottom panel shows the projection of E_x(^{27}Al). Different proton groups are identified and labeled as p_i, representing the protons populating ^{27}Al at the ith excited state. Some of the very energetic α particles from the α_0 channel can leak into the proton group of p_{13} and above where the signals are just above the detection threshold of the silicon detectors.

the HPGe detector at lower energies $E_{\rm beam} \leqslant 11.3$ MeV. While the use of the HPGe detector reduced the total efficiency in the γ detection, it provided better energy resolution for γ rays, resulting in less background.

III. ANALYSIS AND RESULTS

Cross sections for various exit channels in the ^{12}C+^{16} fusion were obtained from the thick-target yields for γ transitions associated with the different decay channels, protons, as well as proton and γ coincident events. The α particles were mostly blocked in the foils in front of the Si detectors, therefore the α channel was only investigated through the subsequent γ decay of the populated states in the ^{24}Mg nucleus. The thick-target reaction yield is obtained from the number of events detected per incident oxygen nucleus on the target for a given reaction channel. It includes the production yield for reactions not only at incident beam energy, but also in the energy range below due to the energy loss of beam particles in the thick HOPG target. The cross section at the incident energy can then be obtained from the derivative dY/dE of the thick-target yields measured in multiple small energy steps [29]. The value of dY/dE at a given energy was determined by fitting the yield in the logarithmic scale at this energy together with the yields detected for the two neighboring energy steps using a second-order polynomial [29]. The partial cross sections are derived from the extracted dY/dE for each of the observed particle groups using the equation

$$\sigma(E) = \frac{1}{\varepsilon}\frac{M_T}{f N_A}\frac{dE}{d(\rho X)}\frac{dY}{dE}, \tag{1}$$

where ε is the detection efficiency of measured γ rays, charged particles, or coincidences, f is the molecular fraction of target nucleus, N_A is Avogadro's constant number, M_T is the molecular weight of the target nucleus, and $dE/d(\rho X)$ is the stopping power calculated with SRIM [30].

The experimental data resulting from the measurement of the ^{12}C(^{16}O, p)^{27}Al reaction are displayed in Fig. 3. Each YY1 detector consists of 16 strips corresponding to different polar angles. Figure 3 (top) shows the proton spectrum in the different strips as a function of excitation energy E_x(^{27}Al) in ^{27}Al after the kinematic correction. The projection of the proton events versus E_x(^{27}Al) is shown in Fig. 3 (bottom). The peaks of proton groups are broad (with a resolution of about 200 keV), reflecting the target thickness as well as angular and kinematic broadening from the 1/4 inch sized beam spot. Nevertheless the p_0 group, corresponding to the population of the ^{27}Al ground state, is well separated from the others. The $p_{1,2}$ group represents the population in the first two excited states at 0.844 and 1.015 MeV. Similarly, the populations in the other low-lying levels (up to p_{12}) can be well identified. Details of these levels are shown in Table I. However, some of the very energetic α particles from the α_0 channel can leak into

TABLE I. The list of known low-lying levels in ^{27}Al from the compilation [28], with comment when observed in the proton spectra or γ decays.

E^* (keV)	J^π	Observed in p spectra?	Observed in γ decays?
0.0	5/2 +	Yes, as p_0	
843.76	1/2 +	Yes, but unresolved as $p_{1,2}$	Yes
1014.56	3/2 +		Yes
2212.01	(7/2 +)	Yes, as p_3	Yes, Doppler shifted
2734.9	5/2 +	Yes, as p_4	Yes, Doppler shifted
2982.00	3/2 +	Yes, but unresolved as $p_{5,6}$	Yes, Doppler shifted
3004.2	(9/2 +)		Yes, Doppler shifted
3680.4	1/2 +	Yes, as p_7	Yes, Doppler shifted
3956.8	3/2 +	Yes, but unresolved as $p_{8,9}$	Yes, Doppler shifted
4054.6	1/2 −		Yes, Doppler shifted
4410.2	5/2 +	Yes, but unresolved as $p_{10,11,12}$	Yes, Doppler shifted
4510.3	(11/2 +)		
4580.0	(7/2 +)		

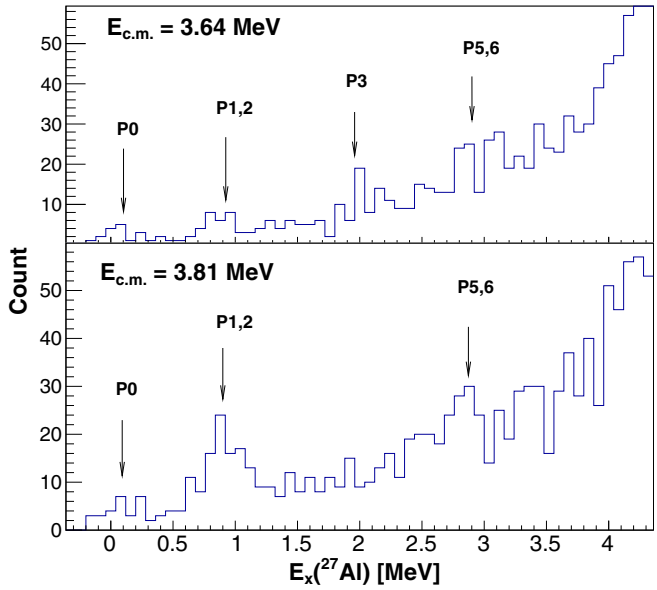

FIG. 4. Proton spectra of ^{12}C(^{16}O, p)^{27}Al reaction are shown for lower energies at $E_{c.m.} = 3.64$ MeV (top panel) and $E_{c.m.} = 3.81$ MeV (bottom panel), respectively. Observed proton groups are labeled as p_i, representing the protons populating ^{27}Al at the ith excited state. The rising trend at the high excitation energy end shows the low energy tail of detected signals contributed from background and noises.

the proton groups of p_{13} and above that corresponds to the low energy signals just above the detection threshold of the silicon detectors. This α leakage may contaminate the spectrum in the very low energy range, therefore no further identification was attempted.

In terms of the direct measurement of the proton channel, the different transitions to excited states in ^{27}Al were successfully measured from the ground state in ^{27}Al up to the sixth excited level, as shown in the proton spectrum (p_0– p_6) of Fig. 3 for the entire energy range covered in this experiment. Figure 4 shows the proton singles data at two of the lowest energy points. The partial cross section of each proton group can be calculated from the thick-target yield following Eq. (1) after correcting for solid angle and angular distribution effects. However, transitions to higher excited states could possibly represent an appreciable fraction of the total cross section for the ^{27}Al + p channel, as suggested by statistical model calculations. Some guidance from statistical model calculations is needed to extract the total cross section of the proton channel.

To complement the partial cross sections measurements of the direct particle population to low lying states that were obtained via charged particle measurements, different cascading sums of partial cross sections were measured via γ ray detection (see Fig. 5). The major γ line of each low lying level gave the cross section including not only the direct population to this level, but also feedings from all the higher lying levels via cascade transitions to that level.

A typical γ spectrum taken at $E_{\text{beam}} = 11.3$ MeV is shown in Fig. 5 as the blue line. The spectrum taken at $E_{\text{beam}} = 7.0$ MeV helps to identify the beam-induced background versus the natural room background, also shown in the figure

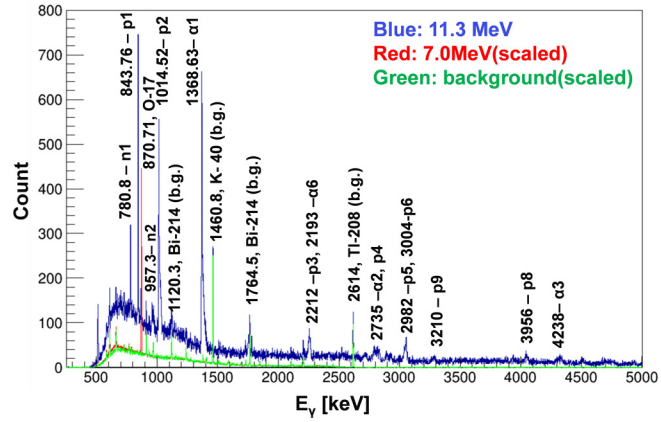

FIG. 5. The HPGe γ-ray spectra taken at $E_{\text{beam}} = 11.3$ MeV (blue) compared with a beam-induced background spectrum at 7.0 MeV (red), and a room background measurement (green). The γ energies and the related particle (n, p, and α) emission channels are labeled for primary γ transitions in ^{12}C + ^{16}O. Some of the pronounced background lines are labeled as well.

as the red line. These spectra are scaled by the incident charge or the duration of the measurement, respectively. The cross sections for single γ transitions are calculated from the thick-target yield after correcting for the efficiency of the detector for each γ energy.

Coincidence data between protons and γ rays are shown in Fig. 6 for a beam energy of $E_{\text{beam}} = 11.3$ MeV. Figure 6(b) shows all γ events taken in coincidence with proton events and Fig. 6(c) indicates the ground state γ transitions from the populated excited states in ^{27}Al. The identified γ rays, such as 843.76 keV from p_1 and 1014.56 keV from p_2, are labeled. Similar spectra are shown in Fig. 7 for beam-induced coincident background measured at an energy of $E_{\text{beam}} = 7.0$ MeV.

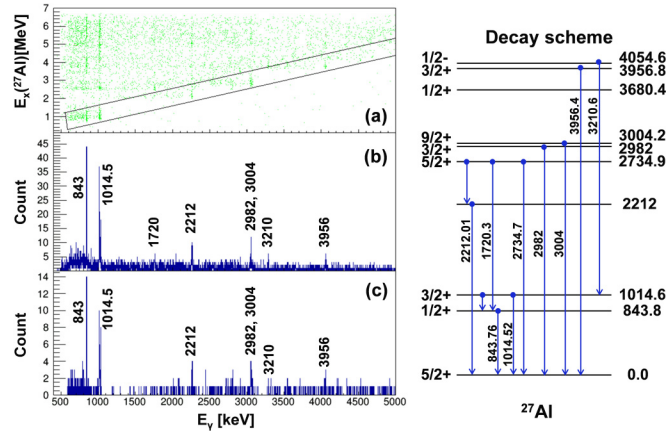

FIG. 6. p-γ coincidences demonstrated for $E_{\text{beam}} = 11.3$ MeV. The top panel (a) displays coincidence events for protons and γ rays, E_x(^{27}Al) vs E_γ. Panel (b) shows the projection of E_γ for all coincident events. Panel (c) shows the projection of E_γ for the coincident events inside the black-box cut indicated in (a). This corresponds to the γ transitions that decay directly from the excited states (with excitation energy up to about 5 MeV) in ^{27}Al to the ground state.

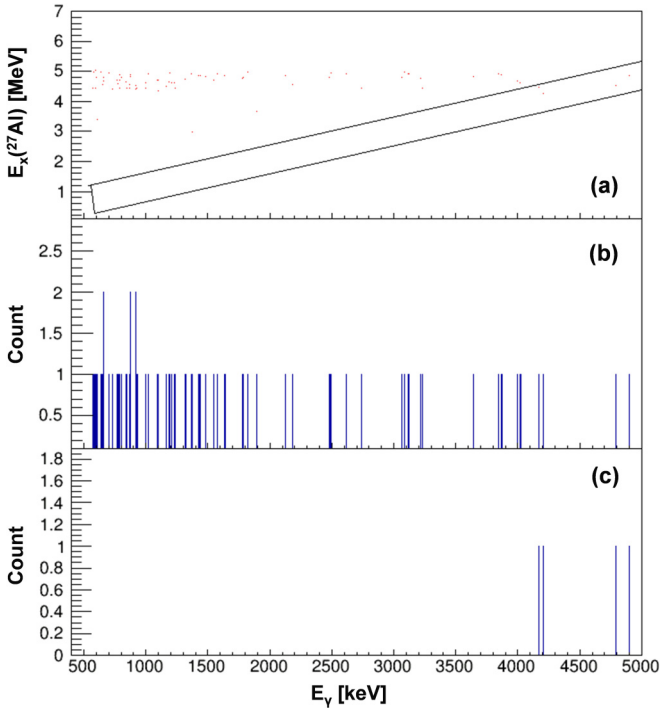

FIG. 7. Beam-induced coincident background taken with the same target at a much lower beam energy $E_{\text{beam}} = 7.0$ MeV is shown. The top panel (a) displays coincidence events for protons and γ rays, equivalent $E_x(^{27}\text{Al})$ vs E_γ. Panel (b) shows the projection of E_γ for all coincident events. Panel (c) shows the projection of E_γ for the coincident events inside the black-box cut indicated in (a). This corresponds to the γ transitions under the same gate as in Fig. 5, i.e., equivalently for direct decays from the excited states (with excitation energy up to about 5 MeV) in ^{27}Al to the ground state.

For comparison and further analysis, the ratios of experimentally determined partial cross sections, or cascading sums of partial cross sections, were compared to predictions from statistical calculations performed with the code SAPPHIRE [31]. The ratios are shown in Fig. 8. SAPPHIRE has been specifically designed to calculate statistical particle and γ-ray distributions arising from the decay of the compound nucleus, in this case ^{28}Si, via the Monte Carlo technique. When adding more contributions from different individual channels to the cross sections, these ratios appear to follow the same overall trend, indicating that the SAPPHIRE calculations provide a reasonably reliable description of relative contributions of the observed individual channels. However, some resonance-like structures that cannot be explained by the calculations are observed in the measurement at energies of roughly about 3.9–4.1, 4.4, and 4.65 MeV, which will be discussed later in this paper.

For the α/n channels of the $^{12}\text{C} + ^{16}\text{O}$ fusion reaction, only γ rays data are presented here since the α particles were stopped in the shielding foil in front of the silicon detectors and no neutrons were measured in this experiment. γ rays with energies of 1369, 2754, 2870, and 4238 keV from the first three excited states in ^{24}Mg and those of 781, 957, 2164, and 1690 keV from the first four excited states in ^{27}Si were measured for the α/n channels, respectively. Similar

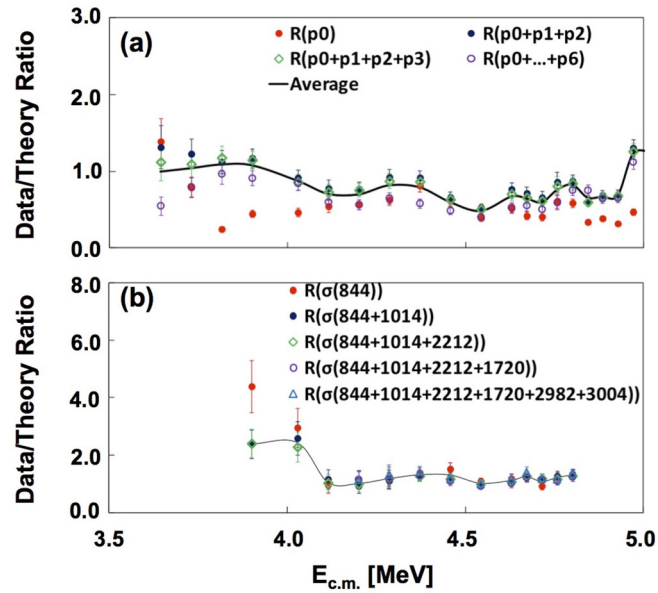

FIG. 8. The ratios of the measured partial cross sections of the $^{27}\text{Al} + p$ channel to those calculated with the statistical model (SAPPHIRE).

comparisons of the γ ray data for the α/n channels with the SAPPHIRE calculations are shown in Fig. 9.

In addition, the relative γ strengths of the observed transitions with respect to the transition of the first excited state to the ground state for all three channels are shown in Fig. 10. The observed ratios are consistent with those calculated with SAPPHIRE. The ratios themselves provide the branchings in the γ cascade of the populated states, a crucial ingredient for the determination of the partial p, α, and n cross sections. By applying the results of the γ-ray measurement and the ratios

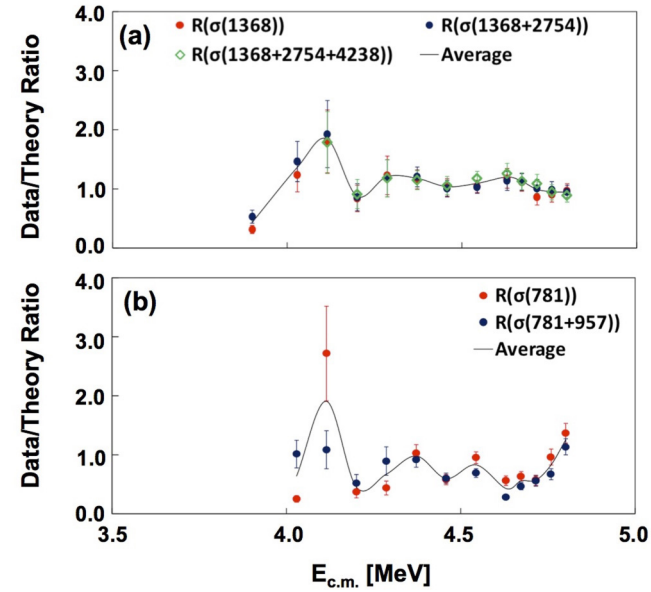

FIG. 9. The ratios of the measured partial cross sections of the $^{24}\text{Mg} + \alpha$ (upper panel) and $^{27}\text{Si} + n$ (lower panel) channels to those calculated with the statistical model (SAPPHIRE).

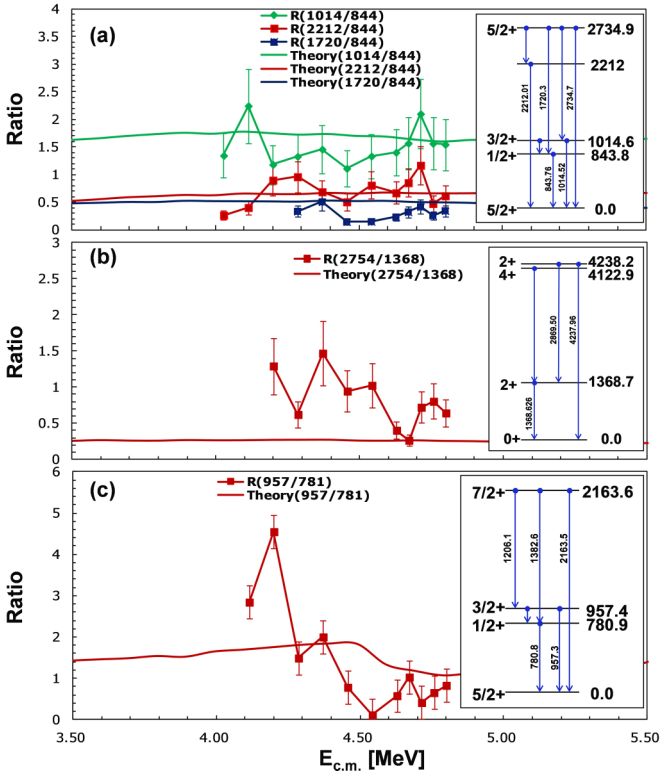

FIG. 10. The relative γ strengths of the observed transitions with respect to the strength of the ground state transition of the first excited state associated with the proton (a), α (b), and neutron (c) channels are shown (symbols). Also shown for comparison are the ratios obtained from the SAPPHIRE calculations (solid lines).

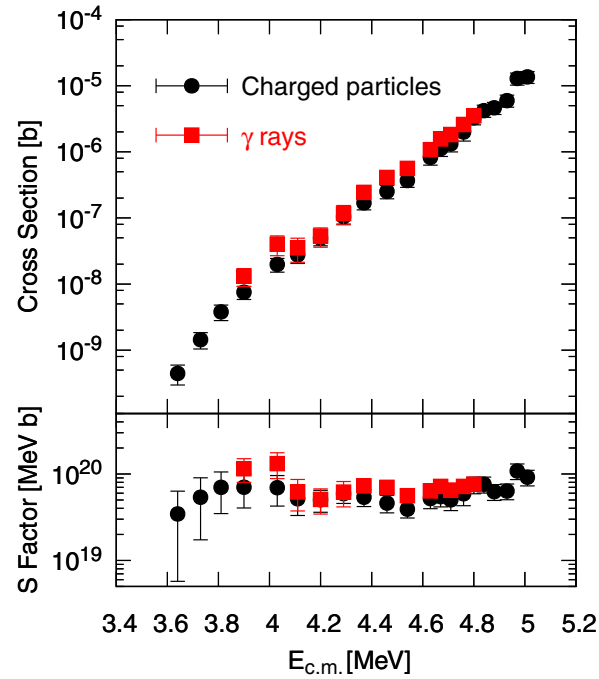

FIG. 11. The total fusion cross section and S factor of the $^{27}Al + p$ channel obtained from the detection of charged particles and γ rays, respectively.

from statistical model calculation, the total cross sections for all three channels, $^{27}Al + p$, $^{24}Mg + \alpha$, and $^{27}Si + n$, were derived.

The consistency, as shown above, between the measured partial cross sections and the calculated ones for the individual observed channels, ensures a reasonable extrapolation of the total cross section by taking into account the missing channels calculated with SAPPHIRE. The total cross section for the $^{27}Al + p$ channel, obtained independently from the charged particles and γ-ray analysis, is shown in Fig. 11 and Table II. The good agreement between the two results further validates the use of SAPPHIRE calculations for providing the missing channels and allowing the determination of the total cross section.

Besides the derivation of the $^{12}C + ^{16}O$ partial cross sections from singles data, this information can also be obtained from the proton-γ coincidence measurement. The coincident channels from the first two excited levels (p_1 and 844 keV, p_2 and 1014 keV) in ^{27}Al were used. The obtained partial cross section was then converted to the total cross section with the aid of statistical calculations to take into account the missing channels, as discussed above.

By summing the partial cross sections of all three open channels, the total fusion cross section of $^{12}C + ^{16}O$ is obtained:

$$\sigma_{\rm tot}(^{12}C + ^{16}O) = \sigma_{p\_\rm tot} + \sigma_{\alpha\_\rm tot} + \sigma_{n\_\rm tot}. \quad (2)$$

The measured partial and total cross sections of $^{12}C + ^{16}O$ are listed in Table III. The uncertainties for high energy data points are dominated by systematic errors of up to 17%, including contributions from detector geometry and efficiency, angular distributions, summing effects, thick target approach, etc. On the other hand, the uncertainties at the lower energy end stem

TABLE II. Measured fusion cross sections of the proton channel $^{12}C(^{16}O, p)^{27}Al$.

$E_{c.m.}$ (MeV)	$\sigma_{p\_\rm tot}$ (proton data) (b)	$\sigma_{p\_\rm tot}$ (γ data) (b)
3.64	$5.06 \pm 3.71 \times 10^{-10}$	
3.73	$1.64 \pm 1.11 \times 10^{-9}$	
3.81	$4.32 \pm 2.17 \times 10^{-9}$	
3.90	$8.57 \pm 3.65 \times 10^{-9}$	$1.31 \pm 0.40 \times 10^{-8}$
4.03	$2.25 \pm 0.87 \times 10^{-8}$	$4.02 \pm 1.33 \times 10^{-8}$
4.11	$3.15 \pm 1.13 \times 10^{-8}$	$3.53 \pm 1.40 \times 10^{-8}$
4.20	$5.63 \pm 1.60 \times 10^{-8}$	$5.33 \pm 1.73 \times 10^{-8}$
4.29	$1.19 \pm 0.28 \times 10^{-7}$	$1.17 \pm 0.38 \times 10^{-7}$
4.37	$1.93 \pm 0.42 \times 10^{-7}$	$2.44 \pm 0.26 \times 10^{-7}$
4.46	$2.87 \pm 0.66 \times 10^{-7}$	$4.09 \pm 0.57 \times 10^{-7}$
4.54	$4.18 \pm 0.88 \times 10^{-7}$	$5.62 \pm 0.58 \times 10^{-7}$
4.63	$9.36 \pm 2.21 \times 10^{-7}$	$1.08 \pm 0.15 \times 10^{-6}$
4.67	$1.28 \pm 0.31 \times 10^{-6}$	$1.57 \pm 0.19 \times 10^{-6}$
4.71	$1.51 \pm 0.37 \times 10^{-6}$	$1.83 \pm 0.26 \times 10^{-6}$
4.76	$2.27 \pm 0.62 \times 10^{-6}$	$2.60 \pm 0.36 \times 10^{-6}$
4.80	$3.72 \pm 0.81 \times 10^{-6}$	$3.51 \pm 0.43 \times 10^{-6}$
4.84	$4.79 \pm 1.01 \times 10^{-6}$	
4.88	$4.64 \pm 0.96 \times 10^{-6}$	
4.93	$5.96 \pm 1.23 \times 10^{-6}$	
4.97	$1.29 \pm 0.26 \times 10^{-5}$	
5.01	$1.36 \pm 0.28 \times 10^{-5}$	

TABLE III. Measured partial and total fusion cross sections of the $^{12}C + {}^{16}O$ reaction.

$E_{c.m.}$ (MeV)	σ_{p_tot} (b)	σ_{α_tot} (b)	σ_{n_tot} (b)	σ_{tot} (b)
3.64	$5.06 \pm 3.71 \times 10^{-10}$			$1.13 \pm 0.83 \times 10^{-9}$
3.73	$1.64 \pm 1.11 \times 10^{-9}$			$3.62 \pm 2.46 \times 10^{-9}$
3.81	$4.32 \pm 2.17 \times 10^{-9}$			$9.50 \pm 4.78 \times 10^{-9}$
3.90	$1.06 \pm 0.27 \times 10^{-8}$	$2.20 \pm 0.45 \times 10^{-9}$		$1.87 \pm 0.48 \times 10^{-8}$
4.03	$2.78 \pm 0.73 \times 10^{-8}$	$1.67 \pm 0.38 \times 10^{-8}$	$4.38 \pm 1.00 \times 10^{-9}$	$4.88 \pm 0.83 \times 10^{-8}$
4.11	$3.30 \pm 0.88 \times 10^{-8}$	$4.19 \pm 1.23 \times 10^{-8}$	$9.13 \pm 2.69 \times 10^{-9}$	$8.40 \pm 1.54 \times 10^{-8}$
4.20	$5.49 \pm 1.17 \times 10^{-8}$	$3.49 \pm 0.93 \times 10^{-8}$	$8.44 \pm 2.26 \times 10^{-9}$	$9.83 \pm 1.52 \times 10^{-8}$
4.29	$1.18 \pm 0.22 \times 10^{-7}$	$8.65 \pm 0.23 \times 10^{-7}$	$2.66 \pm 0.71 \times 10^{-8}$	$2.32 \pm 0.33 \times 10^{-7}$
4.37	$2.30 \pm 0.22 \times 10^{-7}$	$1.56 \pm 0.22 \times 10^{-7}$	$4.94 \pm 0.68 \times 10^{-8}$	$4.36 \pm 0.32 \times 10^{-7}$
4.46	$3.57 \pm 0.43 \times 10^{-7}$	$2.28 \pm 0.33 \times 10^{-7}$	$5.69 \pm 0.82 \times 10^{-8}$	$6.41 \pm 0.55 \times 10^{-7}$
4.54	$5.18 \pm 0.48 \times 10^{-7}$	$3.94 \pm 0.40 \times 10^{-7}$	$1.16 \pm 0.12 \times 10^{-7}$	$1.03 \pm 0.06 \times 10^{-6}$
4.63	$1.04 \pm 0.12 \times 10^{-6}$	$7.28 \pm 1.02 \times 10^{-7}$	$8.15 \pm 1.14 \times 10^{-8}$	$1.84 \pm 0.16 \times 10^{-6}$
4.67	$1.49 \pm 0.16 \times 10^{-6}$	$9.18 \pm 1.18 \times 10^{-7}$	$1.71 \pm 0.22 \times 10^{-7}$	$2.58 \pm 0.20 \times 10^{-6}$
4.71	$1.72 \pm 0.22 \times 10^{-6}$	$1.06 \pm 0.16 \times 10^{-6}$	$2.63 \pm 0.39 \times 10^{-7}$	$3.04 \pm 0.27 \times 10^{-6}$
4.76	$2.51 \pm 0.31 \times 10^{-6}$	$1.31 \pm 0.18 \times 10^{-6}$	$4.03 \pm 0.55 \times 10^{-7}$	$4.23 \pm 0.36 \times 10^{-6}$
4.80	$3.56 \pm 0.38 \times 10^{-6}$	$1.60 \pm 0.19 \times 10^{-6}$	$8.69 \pm 1.03 \times 10^{-7}$	$6.02 \pm 0.43 \times 10^{-6}$
4.84	$4.79 \pm 1.01 \times 10^{-6}$			$9.86 \pm 2.08 \times 10^{-6}$
4.88	$4.64 \pm 0.96 \times 10^{-6}$			$9.53 \pm 1.98 \times 10^{-6}$
4.93	$5.96 \pm 1.23 \times 10^{-6}$			$1.22 \pm 0.25 \times 10^{-5}$
4.97	$1.29 \pm 0.27 \times 10^{-5}$			$2.64 \pm 0.54 \times 10^{-5}$
5.01	$1.36 \pm 0.28 \times 10^{-5}$			$2.79 \pm 0.57 \times 10^{-5}$

mainly from lower statistics and relatively higher background. The uncertainties in Hauser-Feshbach calculations are systematic uncertainties associated with the choice of potential and level density parameters. These uncertainties typically affect the absolute strength of Hauser-Feshbach predictions for cross sections but do not much affect the relative branchings, as in the present case, and are therefore not included in the error evaluation.

This can be compared with previous theoretical estimates and experimental results. Figure 12 shows the ratio of the neutron, α, and proton partial cross sections to the total $^{12}C + {}^{16}O$ fusion cross section. In addition to the observed low energy data, the figure also shows the experimental results of previous measurements by Christensen *et al.* [16] and Patterson *et al.* [17]. Within the given experimental uncertainties the experimental data are consistent with each other. The results demonstrate that the dominant particle channels are the α and proton channels, with an average branching ratio of approximately 40–50% each. These branching ratios fluctuate slightly as a function of energy. The neutron channel has an average contribution of 9%. These results are in good agreement with early estimates of 10% for the neutron channel, 50% for the proton channel, and 40% for the α channel [32].

Traditionally, in nuclear astrophysics the cross section for charged particles is expressed in terms of the astrophysical $S(E)$ factor, which corrects to first order the influence of the Coulomb-barrier for interaction between $\ell = 0$ particles [33] and is given by

$$S(E) = \sigma(E) E\, e^{2\pi\eta}, \tag{3}$$

where $\sigma(E)$ is cross section at the center of mass energy E_{cm} and $\eta = Z_1 Z_2 e^2/(\hbar v)$ is the Sommerfeld parameter. The

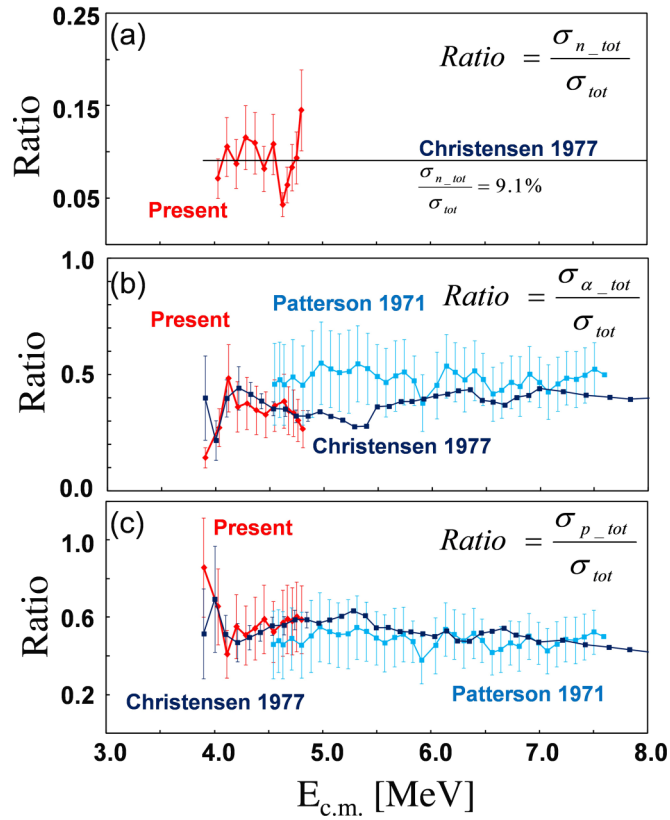

FIG. 12. The ratios of the cross sections of three particle emission channels (n, α, and p) to the total $^{16}O + {}^{12}C$ fusion cross section are shown in panels (a), (b), and (c), respectively. Previous data [16,17] on the p and α channels are shown for comparison. For the n channel, a flat ratio of 9% was used in the data of Christensen *et al.* [16].

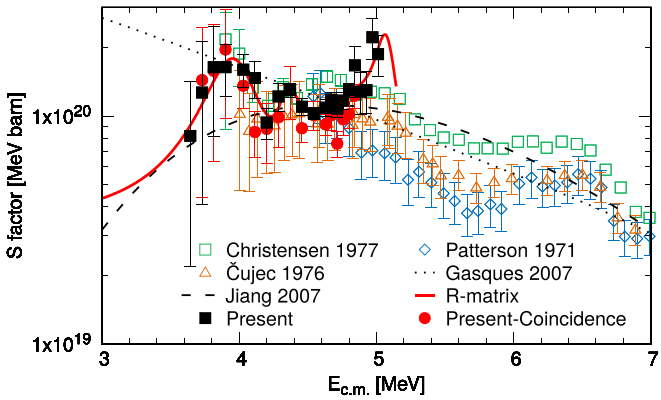

FIG. 13. The $S(E)$ factor of $^{12}C + ^{16}O$ fusion. In addition to the data of the present work (solid symbols) also previous data (open symbols) from the literature [15–17] are shown. Patterson's data [17] does not include the n channel. The dotted line denotes the calculations using the Sao Paulo potential [2,41]. The hindrance model fit [7] with all the data points is presented as the dashed line. An R-matrix calculation (solid line) based on the analysis of the proton channel is shown as well.

$S(E)$ factor therefore represents the nuclear transition strength, higher orders of orbital angular momentum contributions, and in this particular case the effects of deviation from interaction between two point-like particles. An additional term in the exponent was introduced [34] to correct for the latter but is not necessary for the present considerations.

The $S(E)$ factors for the three reaction channels are calculated from the partial cross sections derived as described above. Figure 13 shows the $S(E)$ factor of the $^{12}C + ^{16}O$ fusion reaction as a function of center-of-mass energy. The $S(E)$ factor extracted from the singles data is shown separately from the $S(E)$ factor extracted from the particle-γ coincidence data, with tabulated values listed in Table IV. The two data sets show good agreement with each other within the experimental uncertainties. In the higher energy range the data also agree reasonably well with previous data by Christensen *et al.* [16] while the data from Patterson *et al.* [17] and Čujec *et al.* [15] are slightly lower but in agreement with the overall trend in the S factor.

The data have been described in the framework of different fusion models. The earlier results by Čujec *et al.* [15] and Christensen *et al.* [16] indicated a gradual increase of the $S(E)$ factor towards lower energies as shown in Fig. 13. These data could be described in the framework of the potential model by Michaud and Vogt [35], describing the increase in S factor as "absorption below the barrier. The new data agree within error with these previous observations but suggest a decline in S factor towards even lower energies. Averaging over the variations in S factor, this decline may be due to a hindrance effect in the fusion probability as suggested by Gasques *et al.* [36], Jiang *et al.* [7], and Gasques *et al.* [2]. The data, however, can also be described in terms of an R-matrix fit using the code AZURE2 [37]. The fit is based on the analysis of the different proton channels, normalized to the total S factor. The fit presented here is certainly not unique, due to the experimental uncertainties. It visualizes broad underlying structures which might point to the existence of cluster resonance structures located at 3.9 to 4.0 MeV center-of-mass energy in the $^{12}C + ^{16}O$ compound system. The large error bars of the data lead to considerable uncertainty in the R-matrix fit of the final S factor. The experimental uncertainties are too large to make a conclusive assessment of the nature of the underlying reaction mechanism as either a statistical dominated process or a process featured by profound molecular cluster configurations.

TABLE IV. Measured S factors of the $^{12}C + ^{16}O$ fusion reaction.

$E_{c.m.}$ (MeV)	S factor (singles data) (MeV b)	S factor (coinc. data) (MeV b)
3.64	$8.19 \pm 6.00 \times 10^{19}$	
3.73	$1.27 \pm 0.86 \times 10^{20}$	$1.44 \pm 1.00 \times 10^{20}$
3.81	$1.64 \pm 0.83 \times 10^{20}$	$1.58 \pm 0.95 \times 10^{20}$
3.90	$1.64 \pm 0.42 \times 10^{20}$	$1.96 \pm 0.98 \times 10^{20}$
4.03	$1.60 \pm 0.27 \times 10^{20}$	$1.36 \pm 0.28 \times 10^{20}$
4.11	$1.47 \pm 0.27 \times 10^{20}$	$8.52 \pm 1.95 \times 10^{19}$
4.20	$9.37 \pm 1.44 \times 10^{19}$	$8.79 \pm 2.59 \times 10^{19}$
4.29	$1.22 \pm 0.17 \times 10^{20}$	$9.89 \pm 2.64 \times 10^{19}$
4.37	$1.30 \pm 0.09 \times 10^{20}$	$1.31 \pm 0.35 \times 10^{20}$
4.46	$1.10 \pm 0.09 \times 10^{20}$	$8.85 \pm 1.22 \times 10^{19}$
4.54	$1.03 \pm 0.06 \times 10^{20}$	$1.01 \pm 0.15 \times 10^{20}$
4.63	$1.09 \pm 0.09 \times 10^{20}$	$9.20 \pm 0.95 \times 10^{19}$
4.67	$1.18 \pm 0.09 \times 10^{20}$	$1.01 \pm 0.14 \times 10^{20}$
4.71	$1.08 \pm 0.10 \times 10^{20}$	$7.58 \pm 0.98 \times 10^{19}$
4.76	$1.17 \pm 0.10 \times 10^{20}$	$9.68 \pm 1.43 \times 10^{19}$
4.80	$1.30 \pm 0.09 \times 10^{20}$	$1.02 \pm 0.14 \times 10^{20}$
4.84	$1.67 \pm 0.35 \times 10^{20}$	$1.23 \pm 0.15 \times 10^{20}$
4.88	$1.28 \pm 0.27 \times 10^{20}$	
4.93	$1.30 \pm 0.27 \times 10^{20}$	
4.97	$2.22 \pm 0.46 \times 10^{20}$	
5.01	$1.87 \pm 0.38 \times 10^{20}$	

The R-matrix analysis indicates the existence of quasi-molecular resonance states in the $^{12}C + ^{16}O$ compound system. Quasimolecular resonant states have been observed in the $^{12}C + ^{12}C$ fusion reaction by Almqvist *et al.* [38] and subsequently have been sought in many low energy fusion reactions. For the $^{12}C + ^{16}O$ system Patterson *et al.* [17] pointed out that no such states could be observed below 6 MeV. The present results confirm the observation by Christensen *et al.* [16] of a weak resonance-like structure at 4.7 MeV center-of-mass energy, as reflected in the comparisons of measured cross sections of individual channels to the calculated ones. The present work also strongly indicates the existence of new resonances at 4.4 and 3.9–4.0 MeV. A new explanation for such resonance-like structures was proposed as a result of large spacings and narrow widths in the levels of the formed compound nucleus or lack of resonances [39]. Alternatively these kind of resonances have been interpreted as molecular structures that appear as a consequence of the dynamic fusion process such as demonstrated for the case of the $^{16}O + ^{16}O$ fusion [40]. Further and better measurements below 4.0 MeV are needed to clarify our understanding of the reaction mechanism and the impact of underlying nuclear structure.

TABLE V. Astrophysical reaction rates $N_A\langle\sigma v\rangle$ (in units of $cm^3s^{-1}mol^{-1}$) of the $^{12}C + {}^{16}O$ fusion reaction.

T (GK)	p channel	α channel	n channel	Total	Hindrance [7]	Sao Paulo [2,41]	CF1988 [43]
0.5	5.1×10^{-30}	3.3×10^{-30}	8.8×10^{-31}	9.3×10^{-30}	9.3×10^{-30}	4.7×10^{-28}	3.9×10^{-28}
0.6	1.7×10^{-26}	1.1×10^{-26}	2.9×10^{-27}	3.1×10^{-26}	3.1×10^{-26}	1.0×10^{-24}	8.2×10^{-25}
0.7	1.3×10^{-23}	8.1×10^{-24}	2.2×10^{-24}	2.3×10^{-23}	2.3×10^{-23}	4.6×10^{-22}	3.6×10^{-22}
0.8	3.4×10^{-21}	2.2×10^{-21}	5.8×10^{-22}	6.1×10^{-21}	6.1×10^{-21}	7.1×10^{-20}	5.5×10^{-20}
0.9	4.0×10^{-19}	2.5×10^{-19}	6.6×10^{-20}	7.1×10^{-19}	6.8×10^{-19}	4.9×10^{-18}	3.8×10^{-18}
1.0	2.4×10^{-17}	1.4×10^{-17}	3.8×10^{-18}	4.2×10^{-17}	3.9×10^{-17}	1.9×10^{-16}	1.4×10^{-16}
1.25	7.5×10^{-14}	4.3×10^{-14}	1.1×10^{-14}	1.3×10^{-13}	1.1×10^{-13}	2.6×10^{-13}	2.0×10^{-13}
1.5	2.7×10^{-11}	1.6×10^{-11}	4.1×10^{-12}	4.7×10^{-11}	4.0×10^{-11}	6.4×10^{-11}	5.0×10^{-11}
1.75	2.5×10^{-9}	1.5×10^{-9}	4.1×10^{-10}	4.4×10^{-9}	4.0×10^{-9}	4.9×10^{-9}	4.0×10^{-9}
2.0	9.5×10^{-8}	6.0×10^{-8}	1.7×10^{-8}	1.7×10^{-7}	1.6×10^{-7}	1.7×10^{-7}	1.5×10^{-7}
2.5	2.4×10^{-5}	1.6×10^{-5}	5.3×10^{-6}	4.6×10^{-5}	4.5×10^{-5}	4.2×10^{-5}	4.2×10^{-5}
3.0	1.4×10^{-3}	1.0×10^{-3}	3.5×10^{-4}	2.7×10^{-3}	2.7×10^{-3}	2.5×10^{-3}	2.8×10^{-3}
3.5	3.2×10^{-2}	2.4×10^{-2}	8.6×10^{-3}	6.4×10^{-2}	6.2×10^{-2}	6.1×10^{-2}	7.2×10^{-2}
4.0	3.8×10^{-1}	3.1×10^{-1}	1.1×10^{-1}	7.9×10^{-1}	7.4×10^{-1}	7.6×10^{-1}	8.9×10^{-1}
5.0	1.5×10^{1}	1.4×10^{1}	4.4×10^{0}	3.3×10^{1}	2.9×10^{1}	3.2×10^{1}	3.1×10^{1}
6.0	2.0×10^{2}	1.9×10^{2}	5.8×10^{1}	4.5×10^{2}	4.0×10^{2}	4.5×10^{2}	3.3×10^{2}
7.0	1.4×10^{3}	1.4×10^{3}	3.9×10^{2}	3.1×10^{3}	2.8×10^{3}	3.1×10^{3}	1.9×10^{3}
8.0	5.8×10^{3}	6.4×10^{3}	1.7×10^{3}	1.4×10^{4}	1.3×10^{4}	1.4×10^{4}	7.0×10^{3}
9.0	1.6×10^{4}	2.1×10^{4}	5.3×10^{3}	4.6×10^{4}	4.1×10^{4}	4.6×10^{4}	2.0×10^{4}
10.0	4.7×10^{4}	5.6×10^{4}	1.4×10^{4}	1.2×10^{5}	1.1×10^{5}	1.2×10^{5}	4.6×10^{4}

IV. REACTION RATES

The stellar reaction rate for the $^{12}C + {}^{16}O$ fusion expresses the probability of the reaction taking place in stellar environments of different temperatures. The nuclear reaction rate can be calculated from the reaction cross section $\sigma(E)$, or the $S(E)$ factor representing the reaction probability as function of energy, by integration over the Maxwell-Boltzmann distribution of the interacting particles in a stellar environment of a temperature T. The reaction rate per interacting particle pair is given by

$$N_A\langle\sigma v\rangle = \left(\frac{8}{\pi\mu}\right)^{\frac{1}{2}} \frac{N_A}{(kT)^{\frac{3}{2}}} \int_0^\infty S(E) e^{-(E/kT+2\pi\eta)} dE, \qquad (4)$$

where μ is the reduced mass, N_A is Avogadro's number, and k is Boltzmann's constant. The partial and total reaction rates based on the present work are shown in Table V and rates from previous work are also presented for comparison. The $S(E)$ factor and its energy dependence are the key parameters for determining the reaction rate. As discussed in the previous section, the low energy range of the $S(E)$ factor remains very uncertain, and predictions rely on the extrapolation of existing data in the framework of nuclear reaction models. In the past the $S(E)$ factor was extrapolated by fitting the high energy experimental data [32] using the phenomenological potential model approach by Michaud and Vogt [35], neglecting any possible resonance structure in the data. Figure 13 shows the extrapolation of the experimental $S(E)$ factor using this approach as the dotted line. The new low energy data actually suggest a decrease of the $S(E)$ factor at stellar energies, as compared to previous work; this translates into a reduction of the stellar reaction rate. This decrease might be due to the hindrance factor, which was suggested to reduce the $S(E)$ factor for fusion reactions towards lower energies [42]. In the framework of the reaction rate discussion, the classical potential model approach represents an upper limit for the S-factor extrapolation while the hindrance model provides a lower limit for the extrapolation and therefore the reaction rate, as demonstrated in Fig. 14. The figure shows both the rate calculated from the new data on the basis of the Sao Paulo potential model as well as the rate derived on the assumption of a hindrance effect, normalized to the rate by Caughlan and Fowler [43]. The lower limit for the rate is calculated using a model that maximizes the hindrance effect, as suggested by Jiang *et al.* [7]. The reaction rate based on the R-matrix calculation is in between the two limits, but still handicapped

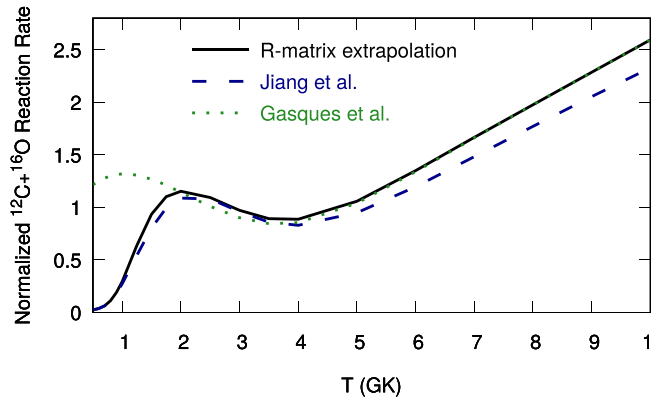

FIG. 14. The reaction rate for the $^{12}C + {}^{16}O$ fusion is shown for both the calculations using the Sao Paulo potential [2,41] (dotted line) and a hindrance model fit [7] (dashed line) of the data, normalized to the standard rate of Caughlan and Fowler [43]. An R-matrix-extrapolation rate (solid line), using the R-matrix fit of the data with high energy extrapolation from the Sao Paulo calculations [2,41] and low energy extrapolation from the hindrance model fit [7], is also shown.

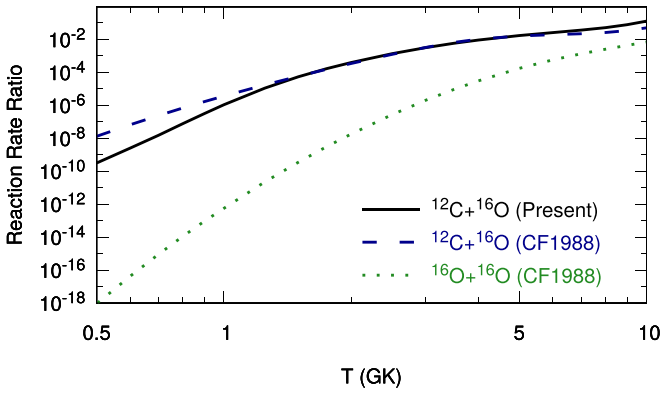

FIG. 15. The past [43] (dashed line) and present (solid line) reaction rates of $^{12}C + ^{16}O$, as well as the rate of $^{16}O + ^{16}O$ [43] (dotted line), are shown normalized to that of $^{12}C + ^{12}C$ fusion [43].

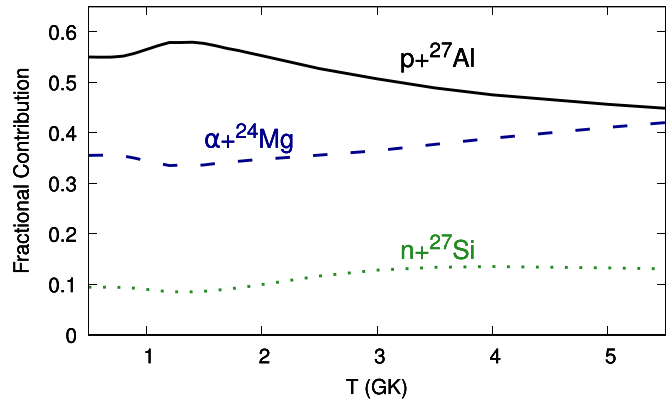

FIG. 16. Fractional contributions of the three main channels of $^{12}C + ^{16}O$ fusion to the astrophysical reaction rate from the present work.

by the large experimental uncertainty and the uncertainty in extrapolation. This is shown in Fig. 14 as the solid line.

The reaction might have an impact in both shell carbon and shell oxygen burning, with reaction products reaching the surface through deep convective processes in the last years of stellar life or as a consequence of shock front driven ejection by a type II core collapse supernova event. Temperatures in shell carbon burning range from 0.9 GK up to 1.2 GK in most of the carbon shell environment. In the final days of carbon burning it could increase to as much as 1.4–1.5 GK, if the shell is still convective. For the oxygen shell, the predictions for the temperatures are very model dependent and turbulence driven mergers with other shells can generate sudden changes [44]. A typical temperature range is around 2.0–2.3 GK. Figure 15 provides a comparison with other fusion rates in carbon and oxygen burning. The figure shows the past and present rates of $^{16}O + ^{12}C$, as well as the fusion rate of $^{16}O + ^{16}O$, normalized to the $^{12}C + ^{12}C$ rate as a function of temperature. This demonstrates that, over the entire temperature regime of carbon burning, the $^{12}C + ^{12}C$ reactions dominates over the competing $^{12}C + ^{16}O$ fusion despite the substantially higher abundance of ^{16}O abundance in the carbon burning regions. For the case of oxygen burning, however, spurious amounts of carbon can already contribute significantly in energy production and nucleosynthesis pattern in the oxygen burning zone. This occurs because the carbon changes both the amount and the distribution of the emitted light particles for redistribution of the ^{28}Si and ^{32}S reaction products of the primary oxygen burning process.

A further aspect for consideration is the branching of the particle channels in the $^{12}C + ^{16}O$ fusion process. The branching of this reaction provides information regarding the quantity of α, proton, and neutron particles released to participate in the nucleosynthesis of heavier nuclei via charged particle and neutron capture reactions. The results are shown in Fig. 16. The figure clearly demonstrates that the dominant channels are the α and proton emission channels, with approximately 45% each, leading to the production of ^{24}Mg and ^{27}Al, respectively. Proton capture on ^{27}Al is dominated by the $^{27}Al(p,\alpha)^{24}Mg$ reaction channel which leads to ^{24}Mg as a major nucleosynthesis product. However α capture on ^{24}Mg is a predominately resonant radiative α capture process [45], which may rapidly convert the material to ^{28}Si and higher mass nuclei at the given temperatures of oxygen burning. The study of the impact requires a network simulation of the nucleosynthesis pattern at oxygen burning conditions. These calculations are beyond the scope of this paper.

V. CONCLUSION

Based on the present data it is not possible to come to a unique assessment of whether or not the low energy $S(E)$ factor is a reflection of a hindrance factor in the nuclear potential or the signature of the existence of quasimolecular states near the threshold energy. More detailed information on the $S(E)$ factor towards even lower energies, and on the energy dependence of the particle branchings, are necessary to come to a conclusive interpretation. For carbon and oxygen core burning conditions of massive stars, the impact is negligible since the size of the stellar core is smaller than the mass cut in the subsequent supernova explosions and the core collapses forming a neutron star. The presently available data also confirm that the reaction plays a negligible role for shell carbon burning since the $^{16}O + ^{12}C$ rate is many orders of magnitude smaller than the dominant $^{12}C + ^{12}C$ fusion process, if one adopts $^{12}C/^{16}O$ abundance predictions from helium burning simulations. In oxygen shell burning, the situation is more complex. While the $^{16}O + ^{12}C$ fusion can strongly compete with the $^{16}O + ^{16}O$ fusion process, the impact on the nucleosynthesis is difficult to predict since the turbulent mixing processes may not only provide fresh fuel material into the burning zone, but may also dilute the reaction products. This effect might be further enhanced by rotation of the pre-supernova star during the last phases of its stellar life [46].

The recent analysis of nucleosynthesis during type Ia supernova explosions [13] indicates that the reaction can play an important role for the Ca/S abundance ratio. The simulations were based on the CF88 rate [43] for the reaction, but the authors demonstrated through extensive simulations that deviations translate directly into variations of the ensuing flux of released α particles, which directly impact the Ca

production. While this experimental work does not lead to a conclusive reaction rate due to the uncertainties in the lower energy range, it provides a realistic uncertainty range within which these kinds of simulation studies can be performed.

ACKNOWLEDGMENTS

We thank Cheng-lie Jiang for the discussions on the hindrance model and Frank Timmes for recent progress on type Ia supernova simulations. This work was supported by the National Science Foundation through Grants No. PHY-1068192 and No. PHY-1419765, the Joint Institute for Nuclear Astrophysics (JINA) under Grant No. PHY-0822648, the Joint Institute for Nuclear Astrophysics–Center for the Evolution of Elements (JINA-CEE) under Grant No. PHY-1430152, the National Natural Science Foundation of China under Grant No. 11775316, and the US Department of Energy under Grant No. DE-FG02-88ER-40404.

[1] M. Pignatari, R. Hirschi, M. Wiescher, R. Gallino, M. Bennett, M. Beard, C. Fryer, F. Herwig, G. Rockefeller, and F. X. Timmes, Astrophys. J. **762**, 31 (2013).
[2] L. R. Gasques, E. F. Brown, A. Chieffi, C. L. Jiang, M. Limongi, C. Rolfs, M. Wiescher, and D. G. Yakovlev, Phys. Rev. C **76**, 035802 (2007).
[3] E. F. Brown and L. Bildsten, Astrophys. J. **496**, 915 (1998).
[4] E. F. Brown, Astrophys. J. **614**, L57 (2004).
[5] B. Nagorcka, G. Symons, W. Zuk, and J. Patterson, Nature (London) **231**, 17 (1971).
[6] N. Cindro, Ann. Phys. Fr. **13**, 289 (1988).
[7] C. L. Jiang, K. E. Rehm, B. B. Back, and R. V. F. Janssens, Phys. Rev. C **75**, 015803 (2007).
[8] M. Wiescher, F. Käppeler, and K. Langanke, Annu. Rev. Astron. Astrophys. **50**, 165 (2012).
[9] S. E. Woosley, W. D. Arnett, and D. D. Clayton, Phys. Rev. Lett. **27**, 213 (1971).
[10] T. A. Weaver and S. E. Woosley, Phys. Rep. **227**, 65 (1993).
[11] L. Buchmann, Astrophys. J. **468**, L127 (1996).
[12] C. A. Meakin and D. Arnett, Astrophys. J. **637**, L53 (2006).
[13] H. Martínez-Rodríguez, C. Badenes, H. Yamaguchi, E. Bravo, F. X. Timmes, B. J. Miles, D. M. Townsley, A. L. Piro, H. Mori, B. Andrews *et al.*, Astrophys. J. **843**, 35 (2017).
[14] B. Bucher, X. Tang, X. Fang, A. Heger, S. Almaraz-Calderon, A. Alongi, A. Ayangeakaa, M. Beard, A. Best, J. Browne *et al.*, Phys. Rev. Lett. **114**, 251102 (2015).
[15] B. Čujec and C. Barnes, Nucl. Phys. A **266**, 461 (1976).
[16] P. R. Christensen, Z. E. Switkowskiw, and R. A. Dayras, Nucl. Phys. A **280**, 189 (1977).
[17] J. R. Patterson, B. Nagorcka, G. Symons, and W. Zuk, Nucl. Phys. A **165**, 545 (1971).
[18] C. L. Jiang, K. E. Rehm, X. Fang, X. D. Tang, M. Alcorta, B. B. Back, B. Bucher, P. Collon, C. M. Deibel, B. DiGiovine *et al.*, Nucl. Instrum. Methods Phys. Res., Sect. A **682**, 12 (2012).
[19] L. Greenwood, K. Katori, R. Malmin, T. Braid, J. Stoltzfus, and R. Siemssen, Phys. Rev. C **6**, 2112 (1972).
[20] T. Rauscher and F.-K. Thielemann, At. Data Nucl. Data Tables **75**, 1 (2000).
[21] W. Hauser and H. Feshbach, Phys. Rev. **87**, 366 (1952).
[22] C. Soldano, A. Mahmood, and E. Dujardin, Carbon **48**, 2127 (2010).
[23] K. Novoselov, A. K. Geim, S. Morozov, D. Jiang, M. Katsnelson, I. Grigorieva, S. Dubonos, and A. Firsov, Nature **438**, 197 (2005).
[24] S. Cernusca, A. Diem, H. Winter, F. Aumayr, J. Lörincik, and Z. Sroubek, Nucl. Instrum. Methods Phys. Res., Sect. B **193**, 616 (2002).
[25] Micron Semiconductor, http://www.micronsemiconductor.co.uk.
[26] G. L. Engel, M. Sadasivam, M. Nethi, J. M. Elson, L. G. Sobotka, and R. J. Charity, Nucl. Instrum. Methods Phys. Res., Sect. A **573**, 418 (2007).
[27] Mesytec, http://http://www.mesytec.com.
[28] M. S. Basunia, Nucl. Data Sheets **112**, 1875 (2011).
[29] M. Notani, H. Esbensen, X. Fang, B. Bucher, P. Davies, C. Jiang, L. Lamm, C. Lin, C. Ma, E. Martin *et al.*, Phys. Rev. C **85**, 014607 (2012).
[30] SRIM code, http://www.srim.org.
[31] M. Beard, E. Uberseder, R. Crowter, and M. Wiescher, Phys. Rev. C **90**, 034619 (2014).
[32] W. A. Fowler, G. R. Caughlan, and B. A. Zimmerman, Annu. Rev. Astron. Astrophys. **13**, 69 (1975).
[33] E. E. Salpeter, Phys. Rev. **88**, 547 (1952).
[34] J. R. Patterson, H. Winkler, and C. S. Zaidins, Astrophys. J. **157**, 367 (1969).
[35] G. Michaud and E. Vogt, Phys. Lett. B **30**, 85 (1969).
[36] L. Gasques, L. C. Chamon, P. Gomes, and J. Lubian, Nucl. Phys. A **764**, 135 (2006).
[37] R. E. Azuma, E. Uberseder, E. C. Simpson, C. R. Brune, H. Costantini, R. J. deBoer, J. Görres, M. Heil, P. J. LeBlanc, C. Ugalde *et al.*, Phys. Rev. C **81**, 045805 (2010); AZURE2 *R*-matrix code, https://azure.nd.edu.
[38] E. Almqvist, D. Bromley, and J. Kuehner, Phys. Rev. Lett. **4**, 515 (1960).
[39] C. L. Jiang, B. B. Back, H. Esbensen, R. V. F. Janssens, K. E. Rehm, and R. J. Charity, Phys. Rev. Lett. **110**, 072701 (2013).
[40] A. Diaz-Torres, L. R. Gasques, and M. Wiescher, Phys. Lett. B **652**, 255 (2007).
[41] D. G. Yakovlev, L. R. Gasques, A. V. Afanasjev, M. Beard, and M. Wiescher, Phys. Rev. C **74**, 035803 (2006).
[42] B. Back, H. Esbensen, C. Jiang, and K. Rehm, Rev. Mod. Phys. **86**, 317 (2014).
[43] G. R. Caughlan and W. A. Fowler, At. Data Nucl. Data Tables **40**, 283 (1988).
[44] W. D. Arnett and C. Meakin, Astrophys. J. **741**, 33 (2011).
[45] E. Strandberg, M. Beard, M. Couder, A. Couture, S. Falahat, J. Görres, P. J. LeBlanc, H. Y. Lee, S. O'Brien, A. Palumbo *et al.*, Phys. Rev. C **77**, 055801 (2008).
[46] E. Chatzopoulos, S. M. Couch, W. D. Arnett, and F. X. Timmes, Astrophys. J. **822**, 61 (2016).